Analysis Model for Magnetic Energy Harvesters

Jinyeong Moon, *Student Member, IEEE*, and Steven B. Leeb, *Fellow, IEEE*

Abstract— **Energy harvesting offers an important design option for creating sensing and control elements without a requirement for custom wiring or batteries. An exciting possibility creates a "self-powered" sensor node with an integrated energy harvester that can extract power from the magnetic fields around a power line to a load, in the manner of a current transformer. However, this "current transformer" provides not just current sensing, but also power for a sensor package, all without ohmic contact. This paper provides a technique for design optimization for maximizing power harvest, revealing a critical result: For any given core in any particular application, power harvest is maximized when the core is permitted to saturate at an opportune time in the line cycle. Circuits for optimizing this power transfer window and experimental results supporting the analysis are presented in this paper.**

Index Terms—**Energy, harvest, inductor, magnetic, nonideal, nonlinear, power, saturation, transfer window, transformer.**

I. INTRODUCTION

FINE grain sensing and control is the future of energy efficiency. Electromechanical systems can waste energy for a variety of reasons. They may be operated poorly. For example, they may be left on when the system does not need to operate, or, when operating, they may be controlled to an inappropriate setpoint. Many electromechanical systems operate under closed-loop feedback control, which can be a disaster for efficient operation in pathological situations. HVAC components, for example, operate to achieve a comfort setpoint, and, without intervention, will continue to do so regardless of a developing but not-yet-crippling failure like the loss of refrigerant charge. Distributed sensing can provide a detailed look at operations, and, with appropriate signal processing, can provide actionable information for preserving mission capability and operational efficiency.

Sensors and control elements require power and communication paths that can quickly create a dizzying requirement for new or additional wiring. Energy harvesting is an important solution to this problem, allowing adequately low-power sensors and controls to operate from power "sources" derived from parasitic or symbiotic energy flows like mechanical vibration [12], [13], [17], thermal gradients [14], [15], acoustic vibrations [16], and light [18]. The research of this paper examines coupling magnetic fields from operating electromechanical equipment like rotating machines to create an inductive energy harvester. This harvester can power sensors for assessing vibration, thermal profile, and other operating signatures that can either indicate diagnostic conditions or affirm proper operation. When possible, inductive coupling can provide a relatively large amount of harvested energy compared to many other approaches, and has the additional benefit of allowing the associated sensor to measure the electrical consumption of the operating electromechanical load.

The heart of the energy harvester presented in this paper is a core-clamp current transformer, as might be used for a current transformer for sensing current. In sensing applications, linearity is important, and core saturation is generally avoided during the design and operation of a magnetic core sensor. Like current sensing, power harvesting occurs in an environment where the core or harvester size is typically constrained. Also, as in the current sensing case, the insertion impedance of the harvester is necessarily low—the harvester should not interfere with the current supplied to a monitored load. However, for energy harvesting, we have found the fascinating result, directly in contrast to the situation for current sensing, that permitting the core of the current transformer to saturate can, in fact, maximize the harvested energy. In magnetic amplifiers [19], magnetic switches [20], [21] or saturable reactor applications, such as [22]–[25], magnetic cores are intentionally saturated during the operation, but they are used for changing the insertion impedance to act as switches, not harvesting power.

References [3]–[8] are recent examples of work exploring the problem of harvesting energy from magnetic fields. Generally, these efforts focus on extracting energy from kinetic motion or vibration, exploiting induction from a magnetic field. For example, [3] discusses a resonance-based vibration energy harvester with air-core coils and permanent magnets, and [4] and [5] perform similar analyses with magnetic cores with higher permeabilities. The references [6]–[8] review the design of vibration or rotation-based magnetic energy harvesters with permanent magnets. These magnetic harvesters in [6]–[8] rely on parasitic inductances to operate boost converters. This paper introduces a harvester that directly couples energy from the magnetic field surrounding a wire, creating a direct electrical transformation with no need for kinetic motion or vibration. The design proposed here is analogous to a classical current sense transformer, but can be used for harvesting useful power for sensors. This approach does not rely on parasitic inductance and does not require a boost converter. It makes direct use of a permeable core as a nonlinear current source to charge a load to a desired level. This approach is distinct in that it exploits the saturation in the core to achieve maximum power harvest, rather than operating in the nonsaturated region as in [6]–[8], for example.

Saturation is highly nonlinear, and this paper presents a model of core behavior, including nonlinearity, that can accurately predict the amount of power harvested from the environs of a current-carrying power wire, e.g., in the terminal connection

Manuscript received March 17, 2014; revised August 12, 2014; accepted September 5, 2014. Date of publication September 12, 2014; date of current version March 5, 2015. Recommended for publication by Associate Editor C. K. Tse.

The authors are with the Department of Electrical Engineering and Computer Science, Massachusetts Institute of Technology, Cambridge, MA 02139 USA (e-mail: jinmoon@mit.edu; sbleeb@mit.edu).

Color versions of one or more of the figures in this paper are available online at http://ieeexplore.ieee.org.

Digital Object Identifier 10.1109/TPEL.2014.2357448

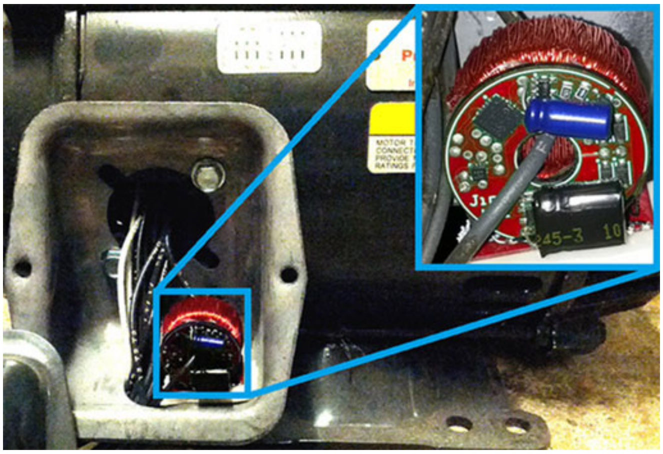

Fig. 1. VAMPIRE physical connection—real example.

box of a motor. Specifically, the model can be used as quick design aids or for more detailed numerical solution to meet an energy harvesting target. The accuracy of this modeling and the efficacy of the harvesting approach through controlled saturation is verified with experimental results.

II. VAMPIRE

We have developed a vibration and temperature monitoring system called VAMPIRE, vibration assessment monitoring point with integrated recovery of energy [1], [2]. VAMPIRE occupies free space in the terminal box of a typical motor enclosure, and can be added "new" or as a retrofit to an existing motor by passing a single-phase wire through a VAMPIRE device. A magnetic core inductively couples energy from the phase wire, similar to a common current transformer but different from that here the goal is to actively extract desired power. While transformers are often operated to avoid saturation, controlled saturation is critical to extracting energy in the harvester application. High core permeability is essential to achieve acceptable winding coupling and adequate harvesting opportunity. Saturation occurs when voltage is intentionally developed on the secondary winding to transfer power. The timing of core saturation with respect to the ac primary side greatly affects the energy recovery. The core saturation complicates analytical modeling, giving rise to a need for a tractable model that can guide design.

Consider the following physical connection as in Fig. 1. The primary side is a single utility phase line at 60 Hz (or 50 Hz), which supplies power to equipment to be monitored, e.g., a motor. The secondary side has N windings and is used to extract energy. The primary side current generates the magnetic field H and the flux density B inside the core, which induces voltage and current on the secondary side. Typically, the insertion impedance of the harvester is relatively low, and the primary wire can be thought as a current source created by the operation of the electromechanical load. If the secondary side carries nonzero current, then it also generates H and affects B inside the core, creating a familiar coupled system. In a steady-state operation, the combined winding system is governed by Maxwell's equations and the *B*–*H* characteristics of the core.

TABLE I
CORE DIMENSIONS

Outer Radius (r_{OD})	12.25 mm
Inner Radius (r_{ID})	8.25 mm
Height (h)	9 mm
Flux Area (A_{CORE})	3.6×10^{-5} m^2
Flux Length (l_{FLUX})	6.44×10^{-2} m

Experiments to validate our analysis procedure were conducted with a magnetic core. High permeability is essential for good coupling prior to saturation, and our illustrative design here uses an amorphous nanocrystalline core (VITROPERM-W380) by Vacuumschmelze (VAC) [9]. The dimensions of this core are listed in Table I.

III. APPROXIMATE POWER HARVESTING ANALYSIS

In normal applications, magnetic cores are operated in a relatively unsaturated region of the *B*–*H* loop. If the core material enters the relatively saturated region in a transformer application, the voltage across the secondary rapidly drops to zero since the voltage that can be developed by the core is proportional to the time derivative of B. In this case, power delivery across the transformer essentially halts. In a current transformer application, if the primary side carries periodic current with sufficient amplitude to create adequate H field to drive the core into saturation, transformer current is transferred into the load only for a portion of the periodic cycle where the core is not saturated. The period of time when the core is able to transfer power might be termed a "transfer window."

The next two sections explore the limits of power harvesting based on the extent of the transfer window. This approach enables quick hand calculations for core size and load target, i.e., an easy "first cut" method for designing a magnetic energy harvester. More accurate numerical analyses for fine-tuning a design are presented in the following sections. For both the approximate and numerical approaches, two possible load types are considered: resistive loads and constant voltage load (with an ideal rectifier, i.e., a regulated dc load).

A. *Resistive Load (R_{LOAD}) Case*

If the primary side current is a sinusoid with frequency of $\omega/2\pi$, the power delivered to the resistor pulsates at twice this frequency. The average power delivered to the load in each half cycle of the primary waveform can be computed given various assumptions about core saturation. The primary side period, the unsaturated time duration (transfer window) in each half cycle, and the time point beginning a half cycle are denoted as T, t_{SAT}, and t_0, respectively. The average power harvest is

$$P_{\mathrm{LOAD}} = \frac{2}{T}\int_{t_0}^{t_0+t_{\mathrm{SAT}}}\left[\frac{I_P}{N}\sin(\omega\, t)\right]^2\cdot R_{\mathrm{LOAD}}\ \mathrm{d}t = \frac{I_P^2\cdot R_{\mathrm{LOAD}}}{\pi\, N^2}\left[\frac{\omega\, t_{\mathrm{SAT}}}{2}-\frac{\sin(2\,\omega\, t_{\mathrm{SAT}})}{4}\right]. \quad (1)$$

When the core does not saturate ($t_{\rm SAT} = T/2$), the average power harvest simply becomes

$$P_{\rm LOAD,nonsat} = \frac{I_P^2 \cdot R_{\rm LOAD}}{2\,N^2}. \tag{2}$$

More generally, the core will saturate. To figure out $t_{\rm SAT}$, a flux equality between the maximally allowed flux set by $B_{\rm SAT}$ for the core and the applied voltage integrated over $T/2$ can be solved. To align the zero crossings of the primary current and the power calculation, the initial time point t_0 is set to 0. Then, the voltage integration is from 0 to $t_{\rm SAT}$

$$\begin{aligned} 2\,B_{\rm SAT}\,A_{\rm CORE}\,N &= \int_0^{t_{\rm SAT}} V_{\rm CORE}(t)\;{\rm d}t \\ &= \int_0^{t_{\rm SAT}} \frac{I_{\rm P}}{N}\,\sin(\omega\,t)\cdot R_{\rm LOAD}\;{\rm d}t. \end{aligned} \tag{3}$$

The coefficient “2” before $B_{\rm SAT}$ on the left-hand side comes from the fact that the core goes from one end of the *B–H* loop to the other end of the *B–H* loop in a half cycle, which results in a net change of $2\,B_{\rm SAT}$. Solving (3) gives

$$t_{\rm SAT} = \min\left[\frac{1}{\omega}\cos^{-1}\left(1 - \frac{2\,\omega\,B_{\rm SAT}\,A_{\rm CORE}\,N^2}{I_P\,R_{\rm LOAD}}\right),\ \frac{T}{2}\right]. \tag{4}$$

Since $t_{\rm SAT}$ is bounded by $T/2$, the minimum $R_{\rm LOAD}$ that saturates the core can be estimated, given $I_{\rm P}$ and N

$$R_{\rm LOAD,min,sat} = \frac{\omega\,B_{\rm SAT}\,A_{\rm CORE}\,N^2}{I_P}. \tag{5}$$

In another special case where the core is heavily saturated, relatively early in the half cycle ($t_{\rm SAT} \ll T/2$), the sinusoidal current in (3) can be approximated as a linear function around zero

$$2\,B_{\rm SAT}\,A_{\rm CORE}\,N \approx \int_0^{t_{\rm SAT}} \frac{I_P}{N}\,\omega\,t\cdot R_{\rm LOAD}\;{\rm d}t. \tag{6}$$

In this hard saturation regime, the expression for $t_{\rm SAT}$ is easily obtained without an inverse cosine function

$$t_{\rm SAT,hardsat} \approx \sqrt{\frac{4\,B_{\rm SAT}\,A_{\rm CORE}\,N^2}{\omega\,I_P\,R_{\rm LOAD}}}. \tag{7}$$

Then, the average power harvest becomes

$$\begin{aligned} P_{\rm LOAD,hardsat} &\approx \frac{2}{T}\int_0^{t_{\rm SAT}} \left[\frac{I_P}{N}\,\omega\,t\right]^2 \cdot R_{\rm LOAD}\;{\rm d}t \\ &= \frac{8}{3\,\pi}\;\frac{\omega^{1.5}\,I_P^{0.5}\,B_{\rm SAT}^{1.5}\,A_{\rm CORE}^{1.5}\,N}{R_{\rm LOAD}^{0.5}}. \end{aligned} \tag{8}$$

Comparing (2) to (8), the two expressions have opposite dependences on $R_{\rm LOAD}$. The harvested power increases with $R_{\rm LOAD}$ in the nonsaturation regime, and decreases with $R_{\rm LOAD}$ in the hard saturation regime. Therefore, it is expected that the peak will occur between two extremes.

Determining the exact $R_{\rm LOAD}$ value for maximum power harvest is challenging because the expression for $P_{\rm LOAD}$ is a complex function of $t_{\rm SAT}$, and $t_{\rm SAT}$ also contains $R_{\rm LOAD}$ inside an inverse cosine function. By finding an extrema using (1) and (4), the following equation set is obtained, which can be solved numerically to find a value for $R_{\rm LOAD}$ that yields maximum power harvest:

$$\begin{cases} R_{\rm LOAD} = \dfrac{2\,\omega\,t_{\rm SAT} - \sin(2\,\omega\,t_{\rm SAT})}{1 - \cos(2\,\omega\,t_{\rm SAT})} \\ \qquad\qquad \times\, \dfrac{\omega\,B_{\rm SAT}\,A_{\rm CORE}\,N^2\,\sin(\omega\,t_{\rm SAT})}{I_P\;[1 - \cos(\omega\,t_{\rm SAT})]^2} \\ t_{\rm SAT} = \dfrac{1}{\omega}\cos^{-1}\left(1 - \dfrac{2\,\omega\,B_{\rm SAT}\,A_{\rm CORE}\,N^2}{I_P\,R_{\rm LOAD}}\right). \end{cases} \tag{9}$$

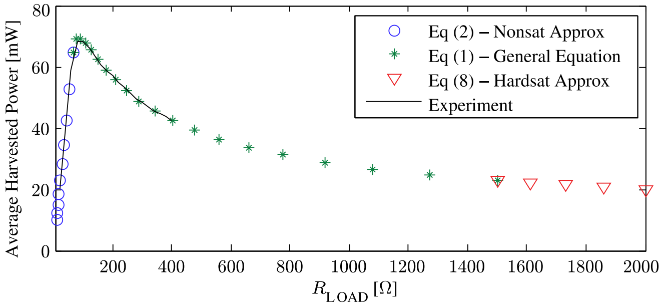

Fig. 2. $P_{\rm LOAD}$ response with a resistive load.

Fig. 2 illustrates an example with $I_P = 6.27\ {\rm A_{RMS}}$, $N = 200$, and freq $= 60 Hz$. In this figure, (8) is verified as a very close approximation to (1) when $R_{\rm LOAD}$ is relatively large, i.e., where the core enters hard saturation. More importantly, the maximum power harvest happens in the soft saturation regime, the region in between the two extremes. The solid black line indicates the experimental result.

B. Constant Voltage Load ($V_{\rm LOAD}$) Case

For powering sensors and signal processing hardware, the energy harvester will likely provide power to a conversion or storage stage, not just a resistor, after a rectification. If a dc–dc converter with a switching frequency much higher than the line frequency is connected to the core as a load, the voltage across the core is effectively the cycle average of the input voltage of the converter, and it can be considered as a constant dc value to the core. Similarly, if a supercapacitor is used, due to its extremely high capacitance and the efforts of a postregulator, the harvester again sees essentially constant dc voltage. In these cases, the important parameter for determining power transfer is the load voltage $V_{\rm LOAD}$.

The calculation of the flux equality is much simpler now due to the time-independent load voltage

$$2\,B_{\rm SAT}\,A_{\rm CORE}\,N = \int_0^{t_{\rm SAT}} V_{\rm LOAD}\;{\rm d}t. \tag{10}$$

Therefore

$$t_{\rm SAT} = \min\left[\frac{2\,B_{\rm SAT}\,A_{\rm CORE}\,N}{V_{\rm LOAD}},\ \frac{T}{2}\right]. \tag{11}$$

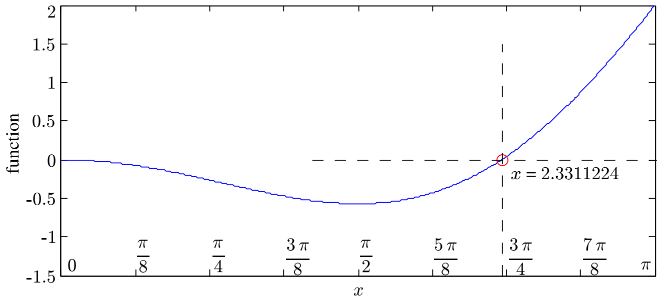

Fig. 3. Trace of $1 - \cos(x) - x \cdot \sin(x)$.

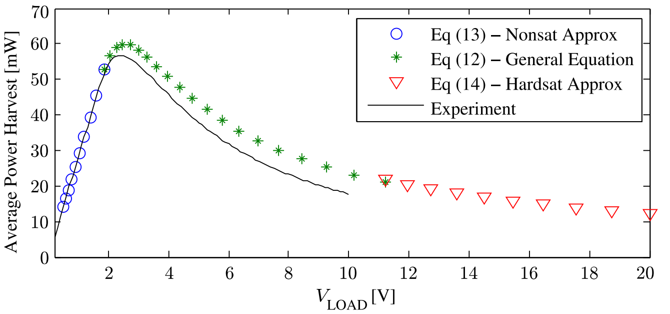

Fig. 4. P_{LOAD} response with a constant voltage load.

The average power harvest can be generally expressed as

$$\begin{aligned} P_{\mathrm{LOAD}} &= \frac{2}{T}\int_0^{t_{\mathrm{SAT}}} \left[\frac{I_P}{N}\sin(\omega\, t)\right]\cdot V_{\mathrm{LOAD}}\ \mathrm{d}t \\ &= \frac{I_P\, V_{\mathrm{LOAD}}}{\pi\, N}\left[1-\cos(\omega\, t_{\mathrm{SAT}})\right]. \end{aligned} \tag{12}$$

Equation (12) can be used to calculate the average power harvest for the special case where the core does not saturate ($t_{\mathrm{SAT}} = T/2$)

$$P_{\mathrm{LOAD,nonsat}} = \frac{2\, I_P\, V_{\mathrm{LOAD}}}{\pi\, N}. \tag{13}$$

The average power harvest in hard saturation ($t_{\mathrm{SAT}} \ll T/2$) is

$$\begin{aligned} P_{\mathrm{LOAD,hardsat}} &\approx \frac{2}{T}\int_0^{t_{\mathrm{SAT}}} \left[\frac{I_P}{N}\,\omega\, t\right]\cdot V_{\mathrm{LOAD}}\ \mathrm{d}t \\ &= \frac{2\,\omega^2\, I_P\, B_{\mathrm{SAT}}^2\, A_{\mathrm{CORE}}^2\, N}{\pi\, V_{\mathrm{LOAD}}}. \end{aligned} \tag{14}$$

Similar to the resistive load case, the expressions for the average power harvest in the two extremes have opposite dependences on the main variable (V_{LOAD} in this case). The peak will occur in between unsaturated and hard saturated operations. The maximum power harvest point is relatively easily found for the case of a voltage load by differentiating P_{LOAD} with respect to V_{LOAD} and solving for extrema

$$\begin{aligned} 0 = \ & 1 - \cos\left(\frac{2\,\omega\, B_{\mathrm{SAT}}\, A_{\mathrm{CORE}}\, N}{V_{\mathrm{LOAD}}}\right) \\ & - \frac{2\,\omega\, B_{\mathrm{SAT}}\, A_{\mathrm{CORE}}\, N}{V_{\mathrm{LOAD}}} \sin\left(\frac{2\,\omega\, B_{\mathrm{SAT}}\, A_{\mathrm{CORE}}\, N}{V_{\mathrm{LOAD}}}\right). \end{aligned} \tag{15}$$

Equation (15) is in the form

$$1 - \cos(x) - x \cdot \sin(x) = 0. \tag{16}$$

This equation has an obvious but impractical solution at $x = 0$. To avoid zero, an additional condition on x can be inferred

$$x = \frac{2\,\omega\, B_{\mathrm{SAT}}\, A_{\mathrm{CORE}}\, N}{V_{\mathrm{LOAD}}} = \omega\, t_{\mathrm{SAT}} \le \omega\, \frac{T}{2} = \pi. \tag{17}$$

Based on (17), the trace of $1 - \cos(x) - x \cdot \sin(x)$ is drawn on Fig. 3 up to $x = \pi$. As shown in the figure, it has a single nonzero solution at $x = 2.33$. Using $3\pi/4$ as an approximate solution, the optimum V_{LOAD} can be expressed as

$$V_{\mathrm{LOAD,pmax}} \approx \frac{8}{3\pi}\cdot \omega\, B_{\mathrm{SAT}}\, A_{\mathrm{CORE}}\, N. \tag{18}$$

The corresponding maximum power harvest is

$$P_{\mathrm{LOAD,max}} \approx \frac{8\,(2+\sqrt{2})}{6\,\pi^2}\cdot \omega\, I_P\, B_{\mathrm{SAT}}\, A_{\mathrm{CORE}}. \tag{19}$$

Fig. 4 illustrates an example with $I_P = 6.27\mathrm{A}_{\mathrm{RMS}}$, $N = 200$, and freq $= 60$ Hz. The maximum power harvest happens in between the unsaturation region and the hard saturation region. The expression of $P_{\mathrm{LOAD,\,max}}$ is independent of the magnetic permeability μ of the core. However, for maximum power transfer, the core must be placed in saturation. Therefore, μ needs to be sufficiently high so that it can drive B from $-B_{\mathrm{SAT}}$ to $+B_{\mathrm{SAT}}$ within the range of the input or primary current. Essentially, high μ improves coupling to the primary current, and permits the soft saturation that is necessary for maximum power harvest in general.

The first-order estimate in Fig. 4 deviates from the experimental observations as the core goes into deeper saturation. This error derives from the fact that the beginning or initiation of the transfer window does not perfectly align with the zero crossing of the primary side current. In (1) and (12), the initial time point of zero in the integral range and the zero-phase angle of the sine function assume a perfect alignment between the beginning of the transfer window and the zero crossing of the primary side current. In practice, the transfer window "opens" earlier than the primary current zero crossing because the core comes out of the saturation ahead of the zero crossing. As soon as the core gets out of the flat tail region of the *B*–*H* loop before the zero crossing, a nonzero slope in the *B*–*H* loop restores magnetizing inductance. Once the magnetizing inductance is restored, the magnetizing current cannot rapidly track the transformer current, and the current difference between them must be flown into the load, opening up the transfer window earlier than before. This nonideality brings significantly different results for the resistive load illustrated in Fig. 2 and the voltage load illustrated in Fig. 4.

For the resistive load, the voltage developed across the core is always proportional to the load current. Therefore, even with a modeling error in estimating the start time of the transfer window, the flux accumulation estimate does not differ greatly, as the voltage and flux accumulation are relatively negligible at the beginning of the transfer window. Therefore, the end point of the transfer window in the estimate does not deviate much from the experiment, showing a similar average power harvest, as in Fig. 2.

On the other hand, for the voltage load case, as soon as the load current exists, the fixed load voltage is applied across the core, and develops core flux at a fixed rate regardless of the level of the transformer current. Therefore, any misestimate in the start time of the transfer window will shift the end time of the transfer window by the same amount. For example, if the transfer window opens early by Δt, the transfer window closes early by the same amount Δt. Since power transfer is relatively low in the vicinity of the zero crossing of the primary sinusoidal current, early opening of the transfer window does little to affect the power harvest. However, early closing of the transfer window will significantly lower the power harvest as substantially higher primary current is flowing after the zero crossing. The worst-case loss happens when the transfer window ends at the peak of the transformer current. This issue tends to be worse in the hard saturation regime because the transfer window is shorter.

The following sections introduce a model to more accurately predict the power harvest in the presence of nonlinearity and other nonidealities.

IV. NONLINEAR MODELING

This section presents a core model that can be used in a numerical solver to predict behavior of the harvester with excellent accuracy. The model, derived from Maxwell's equations, is especially useful for refining a target design. Nonidealities such as hysteresis core loss and wire losses are considered.

A. Maxwell Model

Denoting the secondary side current as $I_S(t)$, the net ampere-turn seen by the core is

$$\mathrm{AT}_{\mathrm{CORE}} = I_P \sin(\omega t) - N \times I_S(t). \tag{20}$$

The primary side current is assumed sinusoidal ac with an amplitude of I_P. The magnetic field $H(r,t)$ in the core is

$$H(r,t) = \frac{\mathrm{AT}_{\mathrm{CORE}}(t)}{2\pi r} = \frac{I_P \sin(\omega t) - N I_S(t)}{2\pi r}. \tag{21}$$

The magnetic flux density B is determined by the *B–H* curve of the core. The preliminary analysis below considers a saturating but nonhysteretic core, followed by an expansion to include hysteresis. Initially, a piecewise linear waveform as in the left of Fig. 5 is used to model saturation. A more refined model uses the "arctan" function as shown on the right of Fig. 5. With the "arctan" function, the magnetic flux density can be modeled as

$$\begin{aligned} B(r,t) &= B_{\mathrm{SAT}} \cdot \frac{2}{\pi} \arctan\left(\frac{H(r,t)}{\alpha}\right) \\ &= B_{\mathrm{SAT}} \cdot \frac{2}{\pi} \arctan\left(\frac{I_P \sin(\omega t) - N I_S(t)}{2\pi r \alpha}\right). \end{aligned} \tag{22}$$

A scale factor of $2/\pi$ is used to normalize the arctan function to 1 when saturated. The reciprocal of α describes the sensitivity in the nonsaturated region, essentially representing the initial permeability in conventional models.

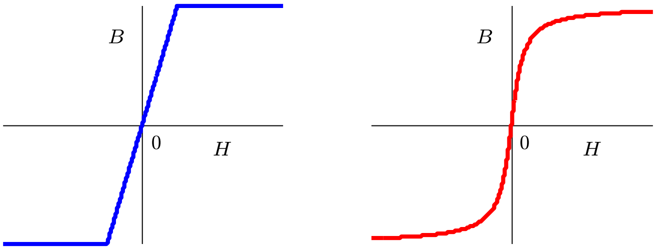

Fig. 5. *B–H* curves with saturation (left: piecewise linear/right: arctan).

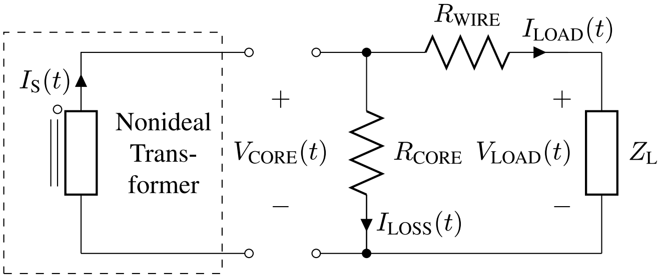

Fig. 6. Circuit representation of Maxwell method.

Denote the height, outer radius, and inner radius of the toroidal core as h, r_{OD}, and r_{ID}, respectively. Voltage across the core is

$$V_{\mathrm{CORE}}(t) = \int_{r_{\mathrm{ID}}}^{r_{\mathrm{OD}}} N \cdot h \cdot \frac{\partial B(r,t)}{\partial t} \mathrm{d}r. \tag{23}$$

The time derivative of the magnetic flux density can be calculated by differentiating (22)

$$\frac{\partial B(r,t)}{\partial t} = \frac{B_{\mathrm{SAT}}}{\pi^2 r \alpha} \cdot \frac{\omega I_P \cos(\omega t) - N \frac{\partial I_S(t)}{\partial t}}{1 + \frac{[I_P \sin(\omega t) - N I_S(t)]^2}{4\pi^2 r^2 \alpha^2}}. \tag{24}$$

Integrating (24) over r from r_{ID} to r_{OD} , (23) can be evaluated

$$\begin{aligned} V_{\mathrm{CORE}}(t) = {} & \frac{N \cdot h \cdot B_{\mathrm{SAT}}}{2\pi^2 \alpha} \times \left[\omega I_P \cos(\omega t) - N \frac{\partial I_S(t)}{\partial t}\right] \\ & \times \ln\left(\frac{r_{\mathrm{OD}}^2 + \frac{[I_P \sin(\omega t) - N I_S(t)]^2}{4\pi^2 \alpha^2}}{r_{\mathrm{ID}}^2 + \frac{[I_P \sin(\omega t) - N I_S(t)]^2}{4\pi^2 \alpha^2}}\right). \end{aligned} \tag{25}$$

B. Loss Modeling

A hybrid circuit representation of (25) is given as a two-port box in a dashed line in Fig. 6. The leakage inductance is relatively small for the experimental core and is ignored in this figure. Wire loss is modeled with R_{WIRE}, which is in series with the load. The effect of hysteresis on the harvester is included with a resistance R_{CORE} in parallel with the core.

Given a load model relating $V_{\mathrm{CORE}}(t)$ and $I_S(t)$, a complete set of differential equations that describes the system can be developed. Assuming the core is connected to an external circuit, a set of general system equations can be obtained by combining (25) and the following equations set:

$$\begin{cases} I_S(t) = I_{\mathrm{LOAD}}(t) + I_{\mathrm{LOSS}}(t) \\ V_{\mathrm{CORE}}(t) = I_{\mathrm{LOSS}}(t) \cdot R_{\mathrm{CORE}} \\ V_{\mathrm{CORE}}(t) = I_{\mathrm{LOAD}}(t) \cdot R_{\mathrm{WIRE}} + V_{\mathrm{LOAD}}(t). \end{cases} \tag{26}$$

First, a resistive load model, i.e., $V_{\mathrm{LOAD}}(t) = I_{\mathrm{LOAD}}(t) \cdot R_{\mathrm{LOAD}}$, is used to demonstrate the analysis technique, with the understanding that the load model can be extended to any load type, including switched loads, given an accurate load model, e.g., an equation relating $V_{\mathrm{LOAD}}(t)$ and $I_{\mathrm{LOAD}}(t)$. The next section illustrates how to model lossy elements R_{WIRE} and R_{CORE}.

1) Wire Loss Modeling: Primary currents for the harvester are typically (but not necessarily) from the power line of monitored equipment operating at line frequency. At 60Hz, the skin depth of the copper wire is

$$\delta = \sqrt{\frac{2\,\rho}{\omega\mu}} = \sqrt{\frac{2 \cdot 1.68 \times 10^{-8}}{2\,\pi\,60 \cdot 4\,\pi \times 10^{-7}}} = 8.42\,\mathrm{mm}. \tag{27}$$

The wire diameter for the secondary windings is usually much smaller than 8.42 mm. For example, in the prototype design, AWG 30 with a diameter of 0.255 mm is used [1]. Because δ is much larger than the wire diameter, the skin effect can be ignored, although this could be important in other applications. Following the analysis discussed in [10] and [11], the proximity effect is also negligible at the line frequency using this wire gauge. As an example, assume AWG 30 with 500 turns and three layers. Each turn is roughly 42.5 mm long, and $R_{\mathrm{DC}} = 7\ \Omega$. To convert the round-wire windings into equivalent foil conductors, each conductor is modeled with $N/3$ windings, and effective height of $2\,\pi\,r_{\mathrm{ID}}$. The effective width of each "foil" is

$$w_{\mathrm{eff}} = \frac{\pi\, r_{\mathrm{AWG30}}^2 \times N/3}{2\,\pi\, r_{\mathrm{ID}}} = 0.164\,\mathrm{mm} \tag{28}$$

and

$$\Delta = \frac{w_{\mathrm{eff}}}{\delta} = 0.0195 \tag{29}$$

with $M = 3$

$$\begin{aligned} F_R = \frac{R_{\mathrm{AC}}}{R_{\mathrm{DC}}} &= \Delta \cdot \left[\frac{\sinh(2\,\Delta) + \sin(2\,\Delta)}{\cosh(2\,\Delta) - \cos(2\,\Delta)} \right. \\ &\quad \left. + \frac{2\,(M^2-1)}{3} \cdot \frac{\sinh(\Delta) - \sin(\Delta)}{\cosh(\Delta) + \cos(\Delta)} \right] \\ &= 1.00000. \end{aligned} \tag{30}$$

Therefore, the proximity effect is negligible, and only dc resistance is required for wire loss modeling.

2) Core Loss Modeling: As will be shown later, hysteresis loss for the VAC core is so low that it can be ignored if the output power is larger than several mW. Here, core loss is discussed to provide a general model for cores with higher losses. Among many techniques to estimate core loss at given frequency and B_{PEAK} level [26]–[31], our core loss model is based on a simple expression of [26] due to zero dc-bias and symmetric *B–H* loop operations centered at zero. The loss in our analysis is proportional to $f^1\,\hat{B}^2$ in principle, though the actual implementation is based on the cyclic measurements of B_{PEAK} and I_{PEAK}.

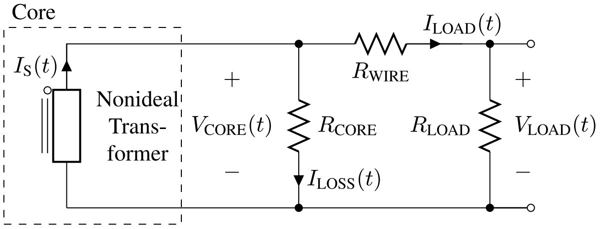

Fig. 7. Test circuit for the parameter estimation.

To model core loss, a rectangular approximation of the *B–H* curve is made since the core has very high initial permeability. The peak load current I_{PEAK}, the peak core voltage (hence B_{PEAK}), and the RMS voltage of the core (V_{RMS}) are tracked in every cycle. These values can be used to estimate a *B–H* loop area. In a numerical simulation, this power loss can be calculated and used to update the resulting core loss resistance for the next cycle. Assuming the core maintains its high permeability until saturation, where Volume is the volume of the core, and H_C is the coercivity of the core, the full hysteresis loss is modeled as

$$P_{\mathrm{LOSS\text{-}MAX}} = 2\,H_C \cdot 2\,B_{\mathrm{SAT}} \cdot \text{Volume} \cdot \text{freq.} \tag{31}$$

The *B–H* loop loss for any particular operating cycle can be calculated as a fraction of the maximum loss

$$P_{\mathrm{LOSS}} = P_{\mathrm{LOSS\text{-}MAX}} \cdot \frac{I_{\mathrm{PEAK}}}{I_{\mathrm{SAT}}} \cdot \frac{B_{\mathrm{PEAK}}}{B_{\mathrm{SAT}}}. \tag{32}$$

Finally, the loss resistance is

$$R_{\mathrm{CORE}} = \frac{V_{\mathrm{RMS}}^2}{P_{\mathrm{LOSS}}}. \tag{33}$$

This model calculation must be performed over a full cycle in order to permit the calculation of the RMS values. The modeled resistor is supposed to dissipate the required amount of power over a cycle (or, if using a rectifier, a half cycle). However, adding such a resistor (or changing the loss resistance) will change the current divider formed with the magnetizing inductance, the core loss resistor, and the load. Since the entire circuit is continuously affected by cyclic update of the loss resistance, an additional numerical solver is used as an "outer loop" to provide a convergence to a correct core loss resistance, operating to provide correct values to the time-domain circuit solver.

C. Parameter Estimation

To demonstrate this model and an approach for a numerical simulation, three parameters are required: B_{SAT}, α, and $P_{\mathrm{LOSS-MAX}}$.

1) B_{SAT} Estimation: The core can be characterized experimentally as shown in Fig. 7, with a resistive load connected to the core. A high load resistance helps characterize the core by forcing the core into hard saturation. In hard saturation, the analysis simplifies because hysteresis loss is at maximum, which ensures that the core is driven to $\pm B_{\mathrm{SAT}}$, and that a distinct "cat-ear" shape in secondary voltage makes it easy to identify the temporal extent of the transfer window.

In a half cycle, $\Delta B = 2\,B_{\mathrm{SAT}}$, hence $\Delta\Lambda = 2\,B_{\mathrm{SAT}}\,A_{\mathrm{CORE}}\,N$. This must be equal to the core voltage integrated over a half cycle. With a measurement of the load voltage over a half cycle

$$\frac{R_{\mathrm{WIRE}}+R_{\mathrm{LOAD}}}{R_{\mathrm{LOAD}}}\cdot V_{\mathrm{LOAD,\,AVG}}\cdot\frac{T}{2}=2\,B_{\mathrm{SAT}}\,A_{\mathrm{CORE}}\,N. \tag{34}$$

Therefore

$$B_{\mathrm{SAT}}=\frac{T\,(R_{\mathrm{WIRE}}+R_{\mathrm{LOAD}})}{4\,A_{\mathrm{CORE}}\,N\,R_{\mathrm{LOAD}}}\cdot V_{\mathrm{LOAD,\,AVG}}. \tag{35}$$

2) $P_{\mathrm{LOSS-MAX}}$ and α Estimation: The same circuit can be used for estimating B_{SAT} to determine core loss, and operate the core in the saturation regime to ensure that the hysteresis loss is at $P_{\mathrm{LOSS-MAX}}$.

With a resistive load, the general system equation set, (25) along with (26), can be simplified to a single equation about $I_{\mathrm{LOAD}}(t)$

$$\frac{N\,h\,B_{\mathrm{SAT}}}{2\,\pi^2\,\alpha}\times\left[\omega\,I_P\cos(\omega\,t)-\gamma\,N\frac{\partial I_{\mathrm{LOAD}}(t)}{\partial t}\right]\times\ln\left(\frac{r_{\mathrm{OD}}^2+\dfrac{[I_P\sin(\omega t)-\gamma\,N\,I_{\mathrm{LOAD}}(t)]^2}{4\,\pi^2\alpha^2}}{r_{\mathrm{ID}}^2+\dfrac{[I_P\sin(\omega t)-\gamma\,N\,I_{\mathrm{LOAD}}(t)]^2}{4\,\pi^2\alpha^2}}\right)=I_{\mathrm{LOAD}}(t)\cdot(R_{\mathrm{WIRE}}+R_{\mathrm{LOAD}}) \tag{36}$$

where γ is defined as

$$\gamma=\frac{R_{\mathrm{CORE}}+R_{\mathrm{WIRE}}+R_{\mathrm{LOAD}}}{R_{\mathrm{CORE}}}. \tag{37}$$

Two equations about α and γ can be generated by evaluating (36) at two different time points. For the evaluations, a full cycle of the primary side current and $V_{\mathrm{LOAD}}(t)$ is captured. The cosine and sine terms can be directly calculated with the selected time points, and $I_{\mathrm{LOAD}}(t)$ can be calculated by $V_{\mathrm{LOAD}}(t)/R_{\mathrm{LOAD}}$. An important point to note is that the zero crossings of the primary side current and $V_{\mathrm{LOAD}}(t)$ do not align in general. Therefore, when evaluating $V_{\mathrm{LOAD}}(t)$ at two time points, the phase shift of $V_{\mathrm{LOAD}}(t)$ with respect to the zero crossing of the primary side should be considered. The variable α, whose reciprocal is practically a scaled initial permeability in conventional models, can be directly obtained by solving the two resulting equations and γ (with $V_{\mathrm{LOAD,RMS}}$ that can be computed with the extracted cycle data) leads to

$$P_{\mathrm{LOAD\text{-}MAX}}=\frac{(\gamma-1)\,V_{\mathrm{LOAD,RMS}}^2}{R_{\mathrm{WIRE}}+R_{\mathrm{LOAD}}}. \tag{38}$$

D. Magnetic Permeability μ_r Estimation

Differentiating both sides of (22) with $H(r,t)$

$$\frac{\partial B}{\partial H}=B_{\mathrm{SAT}}\cdot\frac{2}{\pi}\cdot\frac{1}{\alpha}\cdot\frac{1}{1+\dfrac{H^2}{\alpha^2}}. \tag{39}$$

This equation is maximized when $H(r,t)=0$, and this is by definition the initial magnetic permeability, $\mu_0\,\mu_r$, at zero. Therefore

$$\mu_r=\frac{2\,B_{\mathrm{SAT}}}{\pi\,\alpha\,\mu_0}. \tag{40}$$

Here, a reciprocal of α is officially proved to be a scaled initial permeability. The nonlinear magnetizing inductance arises from the fact that μ_r is an estimate of the initial permeability, and will not be maintained constant throughout the period.

V. NUMERICAL SIMULATION

The numerical circuit simulator is implemented in MATLAB. The multidimensional Jacobian-free numerical solvers employed in the simulator are based on the Newton and the generalized conjugate residual (GCR) [32], [33] methods, and find solutions of equations generated from the Maxwell core model, the core loss model, and the load model. The Newton method is used to find a zero crossing, i.e., solution, of a function, and the GCR is used to rapidly construct the search direction for the next Newton. At each iteration of the GCR, a vector orthogonal to those obtained from earlier iterations is added to the search direction. The progression in time, i.e., estimating the next time point for transient simulation, is modeled by trapezoidal integration.

Consider the resistive load case as an example. Rearranging (36) to get the first time derivative of $I_{\mathrm{LOAD}}(t)$ yields

$$\frac{\partial I_{\mathrm{LOAD}}(t)}{\partial t}=\frac{\omega\,I_P}{\gamma\,N}\cos(\omega t)-\frac{2\pi^2\alpha}{\gamma\,N^2\,h\,B_{\mathrm{SAT}}}\times\frac{(R_{\mathrm{WIRE}}+R_{\mathrm{LOAD}})\cdot I_{\mathrm{LOAD}}(t)}{\ln\left(\dfrac{r_{\mathrm{OD}}^2+\dfrac{[I_P\sin(\omega t)-\gamma\,N\,I_{\mathrm{LOAD}}(t)]^2}{4\,\pi^2\alpha^2}}{r_{\mathrm{ID}}^2+\dfrac{[I_P\sin(\omega t)-\gamma\,N\,I_{\mathrm{LOAD}}(t)]^2}{4\,\pi^2\alpha^2}}\right)}. \tag{41}$$

Trapezoidal integration applied to $I_{\mathrm{LOAD}}(t)$ results in a discrete-time approximation

$$I_{\mathrm{LOAD}}(t_{n+1})-I_{\mathrm{LOAD}}(t_n)=\frac{1}{2}\,\Delta t\left(\left.\frac{\partial I_{\mathrm{LOAD}}(t)}{\partial t}\right|_{t=t_n}+\left.\frac{\partial I_{\mathrm{LOAD}}(t)}{\partial t}\right|_{t=t_{n+1}}\right). \tag{42}$$

Equations (41) and (42) can be combined to move all the terms to the same side, which is equated to G. The equation $G=0$ can be numerically solved using Newton with GCR for each time point. The first-order differential equation requires one initial condition. Since the primary side is a sine wave, its value is zero at $t=0$, and if the system is fully deenergized, $I_{\mathrm{LOAD}}(t)$ is zero as well. This initial condition produces a turn-on transient. After obtaining $I_{\mathrm{LOAD}}(t)$ for the entire cycle, I_{PEAK}, B_{PEAK}, and $V_{\mathrm{CORE,\,RMS}}$ are calculated. Using the same steps discussed in (32) and (33), P_{LOSS} and R_{CORE} can be obtained.

```
Until($|F_{\mathrm{SHOOTING}}| \leq$ Tolerance for $F$) {
   for each time point $\tau$ {
      Until($|G| \leq$ Tolerance for $G$) {
         Newton_GCR on G;(residual update)
      }
      $I_{\mathrm{LOAD}}(\tau)$ = Solved Value;
   }
   $V_{\mathrm{CORE,RMS}}$ Calculation;
   $P_{\mathrm{LOSS}}$ Calculation;
   Newton_GCR on F;(residual update)
}
```

Fig. 8. Pseudocode of the numerical simulator.

TABLE II
CORE PARAMETERS

B_{SAT}	1.190 T
$P_{\mathrm{LOSS\text{-}MAX}}$	0.125 mW
α	2.2

Two challenges for predicting power harvest remain: first, we seek power harvesting capability in steady state, not during the initial transient; second, the convergence of the values for R_{CORE} and $V_{\mathrm{CORE,RMS}}$ is not yet characterized. In order to guarantee convergence to a steady-state solution in the presence of core loss, a second solver with a shooting function F_{SHOOTING} is required; this solver returns a 2×1 vector. The added solver also employs Newton with GCR, and wraps around the time range solver. The first element of the shooting function calculates the difference of two function values that are separated by a period in time, and returns zero if the solution is in steady state:

$$F_{\mathrm{SHOOTING}}[1] = I_{\mathrm{LOAD}}(t_0 + T) - I_{\mathrm{LOAD}}(t_0). \tag{43}$$

The second element of F_{SHOOTING} calculates the difference between two core loss resistance values in two consecutive iterations. If the difference converges to zero, R_{CORE}, P_{LOSS}, and $V_{\mathrm{CORE,RMS}}$ are in a correct relationship. $R_{\mathrm{CORE\text{-}PREV}}$ denotes the core loss resistance calculated in the previous iteration

$$F_{\mathrm{SHOOTING}}[2] = \frac{V_{\mathrm{CORE,RMS}}^2}{P_{\mathrm{LOSS}}} - R_{\mathrm{CORE\text{-}PREV}}. \tag{44}$$

If $|F_{\mathrm{SHOOTING}}|$ is within the tolerance, the system is in the steady state, and the core loss is correctly estimated. Fig. 8 describes the pseudocode including two solvers in separate layers and the shooting function.

VI. EXPERIMENTS AND SIMULATION RESULTS

An amorphous nanocrystalline core was used to verify the validity of the proposed modeling and analysis. The estimated parameter values, B_{SAT}, $P_{\mathrm{LOSS\text{-}MAX}}$, and α, of the VAC core are listed in Table II.

In Fig. 9, four plots are presented to summarize the close agreement between the experiments and the simulation results of the Maxwell modeling method described in the previous sections.

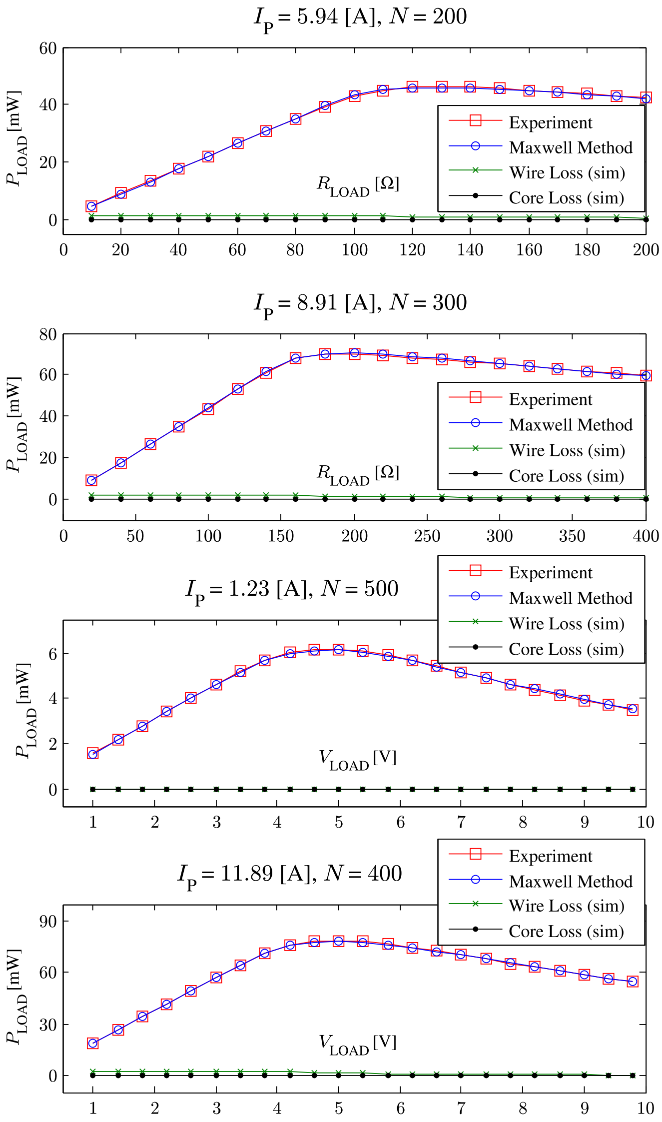

Fig. 9. Experimental verification of the Maxwell modeling method.

The first two plots of Fig. 9 illustrate the resistive load case in two different combinations of I_P and N. The remaining plots illustrate the constant voltage load case in two different combinations of I_P and N. The experimental results (red) and simulation results (blue) are almost identical in all configurations, indicating that the modeling accurately represents physical responses of the core under various settings of load type I_P and N. The experiments also demonstrate that every power delivery peak happens after the linear—unsaturated—region. Therefore, power harvest is maximized when the core is loaded sufficiently to cause saturation. In other words, controlling the level and timing of saturation of the core is crucial to extract the maximum magnetic energy from a sinusoidal primary current.

The results of the wire and core loss simulation are also overlaid in the plots. The ratio of wire loss to the power harvest can be substantial in nonsaturated operation where the transformer current is delivered into the load for the entire cycle. However, the amount of power harvest in the nonsaturated region is

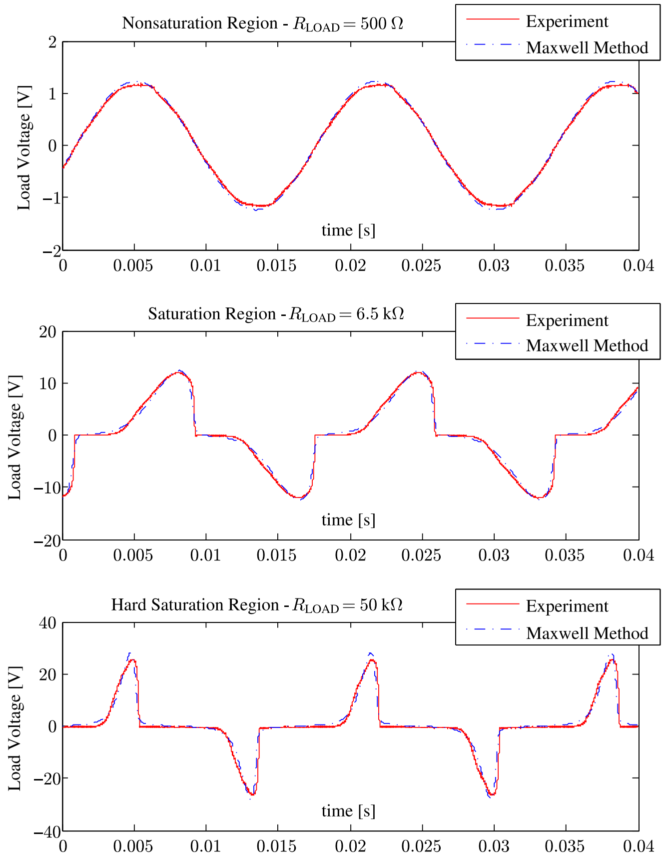

Fig. 10. Load voltage waveforms in experiments ($I_P = 1.23$ A, $N = 500$).

suboptimal, rendering the power harvest lower than what could have been achieved by allowing the core to saturate. Therefore, by taking the maximum power harvest point, the ratio of wire loss to the power harvest can be greatly reduced. Furthermore, at the maximum power harvest point, the core goes into saturation. The transfer window is shortened, and the RMS current is lowered, further reducing wire loss. Therefore, wire loss can be considered negligible when operating at the maximum power harvest point. For example, at the maximum power harvest point in the fourth plot of Fig. 9, the power harvest is 78.62 mW, and the wire loss is 1.38 mW (1.76%). The core loss is negligible because the amorphous nanocrystalline core that is employed in this paper has very low hysteresis loss at line frequency ($P_{\text{LOSS-MAX}} = 0.125$ mW).

Fig. 10 presents time-domain comparisons between the experiments and the simulations of Maxwell method, where the waveforms of the load voltage in the resistive load case are depicted for three different saturation and load conditions.

VII. CONCLUSION

This paper demonstrates that quick approximations can identify the transfer window for power transfer in a magnetically saturating current-driven core. This quick analysis can be used for reasonably accurate decisions on core sizing and load targets for the magnetic energy harvester. A more accurate core model based on Maxwell's equations has been presented for precise numerical design simulation, where the B–H curve of the core material is modeled and nonideal losses are considered. Parameter estimation techniques for the magnetic core are demonstrated, and the numerical solver using Newton with GCR is presented. The solver has two layers: the first being the time range solver; and the second being the steady-state and core loss consistency solver. Experimental results demonstrate that the proposed modeling method is accurate both in predictions of amount of power harvest and in time-domain waveforms, across various operating points as well as different loading conditions.

Operating the harvester at typical utility line frequency, the winding loss from the proximity effect and the skin effect can be ignored, and the wire loss is solely caused by the dc resistance, which also can be ignored if the core is operating near the maximum power harvest point. Using an amorphous nanocrystalline core with low hysteresis loss, the core loss also can be omitted from the analysis. Finally, an exciting and counter-intuitive point can be drawn from the results: the power harvest is maximized when the core is placed in saturation. Therefore, controlling the level and the timing of saturation of the core is crucial to achieve the maximum power harvest from an inductively coupled current-driven magnetic core.

ACKNOWLEDGMENT

The authors would like to thank the Kwanjeong Educational Foundation, the Office of Naval Research Structural Acoustics Program and Debbie Nalchajian, and The Grainger Foundation.

REFERENCES

[1] J. Moon, J. Donnal, J. Paris, and S. Leeb, "VAMPIRE: A magnetically self-powered sensor node capable of wireless transmission," in *Proc. 28th Annu. IEEE Appl. Power Electron. Conf. Expo.*, Mar. 2013, pp. 3151–3159.

[2] J. Donnal, U. Orji, C. Schantz, J. Moon, and S. Leeb, "VAMPIRE: Accessing a life-blood of information for maintenance and damage assessment," in *Proc. Amer. Soc. Naval Eng.*, Feb. 2012, pp. 820–830.

[3] R.Dayal, S. Dwari, and L.Parsa, "A new design for vibration-based electromagnetic energy harvesting systems using coil inductance of microgenerator," in *IEEE Trans. Ind. Appl.*, vol. 47, no. 2, pp. 820–830, Mar./Apr. 2011.

[4] X. Xing, J. Lou, G. Yang, O. Obi, C. Driscoll, and N. Sun, "Wideband vibration energy harvester with high permeability magnetic material," *Appl. Phys. Lett.*, vol. 95, no. 13, pp. 1341031–1341033, Sep. 2009.

[5] X. Xing, G. Yang, M. Liu, J. Lou, O. Obi, and N. Sun, "High power density vibration energy harvester with high permeability magnetic material, " *J. Appl. Phys.*, vol. 109, pp. 07E5141–07E5143, Feb. 2011.

[6] Q. Sun, S. Patil, S. Stoute, N. Sun, and B. Lehman, "Optimum design of magnetic inductive energy harvester and its AC-DC converter," in *Proc. Energy Convers. Congr. Expo.*, Sep. 2012, pp. 394–400.

[7] Q. Sun, S. Patil, N. Sun, and B. Lehman, "Modeling and optimization of an inductive magnetic harvester considering nonlinear effects," in *Proc. Control Modeling Power Electron.*, Jun. 2013, pp. 1–6.

[8] Q. Sun, S. Patil, N. Sun, and B. Lehman, "Inductive magnetic harvester with resonant capacitive rectifier based on synchronized switch harvesting technique," in *Proc. IEEE Energy Convers. Congr. Expo.*, Sep. 2012, pp. 394–400.

[9] G. Herzer, "Amorphous and nanocrystalline soft magnets," in *Proc. NATO Adv. Study Inst.*, vol. 338, pp. 711–730, Jul. 1996.

[10] P. Dowell, "Effects of eddy currents in transformer windings," *Proc. IEE*, vol. 113, no. 8, pp. 1387–1394, Aug. 1966.

[11] W. Hurley, "Optimizing the AC resistance of multilayer transformer windings with arbitrary current waveforms," *IEEE Trans. Power Electron.*, vol. 15, no. 2, pp. 369–376, Mar. 2000.

[12] S. Meninger, J. Mur-Miranda, R. Amirtharajah, A. Chandrakasan, and J. Lang, "Vibration-to-electric energy conversion," *IEEE Trans. Very Large Scale Integr. Syst.*, vol. 9, no. 1, pp. 64–76, Feb. 2001.

[13] G. Ottman, H. Hofmann, A. Bhatt, and G. Lesieutre, "Adaptive piezoelectric energy harvesting circuit for wireless remote power supply," *IEEE Trans. Power Electron.*, vol. 17, no. 5, pp. 669–676, Sep. 2002.

[14] I. Stark, "Thermal energy harvesting with thermo life," in *Proc. IEEE Int. Workshop Wearable Implantable Body Sens. Netw.*, Apr. 2006, pp. 19–22.

[15] Y. Tan and S. Panda, "Energy harvesting from hybrid indoor ambient light and thermal energy sources for enhanced performance of wireless sensor nodes," *IEEE Trans. Ind. Electron.*, vol. 58, pp. 4424–4435, Sep. 2011.

[16] A. Fowler, S. Moheimani, and S. Behrens, "A 3-DoF MEMS ultrasonic energy harvester," *presented at the IEEE Sens.*, Taipei, Taiwan, pp. 1–4, Oct. 2012.

[17] J. Paradiso and T. Starner, "Energy scavenging for mobile and wireless electronics," *IEEE Pervasive Comput.*, vol. 4, no. 1, pp. 18–27, Jan. 2005.

[18] D. Brunelli, C. Moser, L. Thiele, and L. Benini, "Design of a solarharvesting circuit for batteryless embedded systems," *IEEE Trans. Circuits Syst. I, Reg. Papers*, vol. 56, no. 11, pp. 2519–2528, Nov. 2009.

[19] P. Mali, *Magnetic Amplifiers—Principles and Applications*. New York, NY, USA: Rider, 1960.

[20] S. Kim, J. Park, S. Choi, Y. Kim, and M. Ehsani, "Optimal control method of magnetic switch used in high-voltage power supply," *IEEE Trans. Power Electron.*, vol. 28, no. 3, pp. 1065–1071, Mar. 2013.

[21] S. Kim and M. Ehsani, "Control and analysis of magnetic switch reset current in pulsed power systems," *IEEE Trans. Power Electron.*, vol. 29, no. 2, pp. 529–533, Feb. 2014.

[22] R. Watson and F. Lee, "Analysis, design, and experimental results of a 1-kW ZVS-FB-PWM converter employing magamp secondary-side control," *IEEE Trans. Ind. Electron.*, vol. 45, no. 5, pp. 806–814, Oct. 1998.

[23] E. da Silva, S. Abeyratne, and Y. Murai, "PWM series resonant DC-link converter with current clamping by the use of saturable core," *IEEE. Trans. Power Electron.*, vol. 14, no. 1, pp. 82–89, Jan. 1999.

[24] H. Gruening, K. Koyanagi, and M. Mukunoki, "Low reverse-recovery stress in high-power converters achieved by self-resetting saturable cores," *IEEE. Trans. Ind. Appl.*, vol. 45, no. 1, pp. 232–238, Jan. 2009.

[25] S. Aldhaher, P. Luk, and J. Whidborne, "Tuning class E inverters applied in inductive links using saturable reactors," *IEEE Trans. Power Electron.*, vol. 29, no. 6, pp. 2969–2978, Jun. 2014.

[26] E. Snelling, *Soft Ferrites—Properties and Applications*. 2nd ed. London, U.K.: Butterworth, 1988.

[27] J. Li, T. Abdallah, and C. Sullivan, "Improved calculation of core loss with nonsinusoidal waveforms," in *Proc. Ind. Appl. Soc. Conf.*, Oct. 2001, vol. 4, pp. 2203–2210.

[28] K. Venkatachalam, C. Sullivan, T. Abdallah, and H. Tacca, "Accurate prediction of ferrite core loss with nonsinusoidal waveforms using only Steinmetz parameters," *Proc. IEEE Comput. Power Electron. Conf.*, Jun. 2002, pp. 36–41.

[29] Y. Han, G. Cheung, A. Li, C. Sullivan and D. Perreault, "Evaluation of magnetic materials for very high frequency power applications," *IEEE Trans. Power Electron.*, vol. 27, no. 1, pp. 425–435, Jan. 2012.

[30] J. Muhlethaler, J. Biela, J. Kolar, and A. Ecklebe, "Core losses under the DC bias condition based on Steinmetz parameters," *IEEE Trans. Power Electron.*, vol. 27, no. 2, pp. 953–963, Feb. 2012.

[31] J. Muhlethaler, J. Biela, J. Kolar, and A. Ecklebe, "Improved core-loss calculation for magnetic components employed in power electronic systems," *IEEE Trans. Power Electron.*, vol. 27, no. 2, pp. 964–973, Feb. 2012.

[32] S. Eisenstat, H. Elman, and M. Schultz, "Variational iterative methods for nonsymmetric systems of linear equations," *SIAM J. Numer. Anal.*, vol. 20, no. 2, pp. 345–357, Apr. 1983.

[33] Y. Saad, *Iterative Methods for Sparse Linear Systems*, 2nd ed. Philadelphia, PA, USA: SIAM, 2003.

Jinyeong Moon (S'12) received the B.S. degree in electrical engineering and computer science from Korea Advanced Institute of Science and Technology, Daejeon, Korea, in 2005, and the M.S. degree in electrical engineering from Stanford University, Stanford, CA, USA, in 2007. He is currently working toward the Ph.D. degree in electrical engineering and computer science at Massachusetts Institute of Technology, Cambridge, MA, USA.

He worked at Hynix Semiconductor, Inc., from 2007 to 2011 as a Senior Research Engineer, designing circuits for DDR4 SDRAM. Since 2011, he has been with the Research Laboratory of Electronics and the Laboratory for Electromagnetic and Electronic Systems at the Massachusetts Institute of Technology. His research interests include modeling, design, and analysis of circuits and systems in the fields of power conversion, energy harvesting, electromagnetics, and renewable energy.

He received the Kwanjeong Scholarship since 2011. He was the grand prize winner in the MIT Clean Energy Prize 2014, and received the Hynix Strategic Patent Award in 2010. He has authored 17 registered U.S. and international patents.

Steven B. Leeb (S'89–M'91–SM'01–F'07) received the Ph.D. degree from the Massachusetts Institute of Technology, Cambridge, MA, USA, in 1993.

He has served as a Commissioned Officer in the USAF reserved, and he has been a Member on the MIT Faculty in the Department of Electrical Engineering and Computer Science, since 1993. He also holds a joint appointment in MITs Department of Mechanical Engineering. He currently serves as MacVicar Fellow and Professor of Electrical Engineering and Computer Science in the Laboratory of Electromagnetic and Electronic Systems. In his capacity as a Professor at MIT, he is concerned with the design, development, and maintenance processes for all kinds of machinery with electrical actuators, sensors, or power electronic drives. He is the author or coauthor of more than 100 publications and 15 U.S. patents in the fields of electromechanics and power electronics.